Evaluation of a compact multi-contrast and multi-resolution X-ray phase contrast edge illumination system for small animal imaging

A compact X-ray edge illumination system

Lorenzo Massimi
Department of Medical Physics and Biomedical Engineering, University College London, Gower Street, London WC1E 6BT, UK

Jeffrey A. Meganck*
Research and Development, Life Sciences Technology, PerkinElmer, Hopkinton, USA

Rebecca Towns
Biological Services, University College London, Gower Street, London WC1E 6BT, UK

Alessandro Olivo
Department of Medical Physics and Biomedical Engineering, University College London, Gower Street, London WC1E 6BT, UK

Marco Endrizzi
Department of Medical Physics and Biomedical Engineering, University College London, Gower Street, London WC1E 6BT, UK

email: l.massimiphd@gmail.com

* Current address: Boston Scientific, Marlborough, USA

Abstract

Purpose: In this work the performance of a compact multi-resolution and multi-contrast X-ray phase system based on edge illumination is investigated. It has been designed for small animal imaging and with a limited footprint for ease of deployment in laboratories.

Methods: The presented edge illumination system is based on a compact microfocus tungsten X-ray source combined with a flat panel detector. The source has a maximum output of 10 W when the minimum spot size of about 15 μm is used. The system has an overall length of 70 cm. A new double sample mask design, obtained by arranging both skipped and non-skipped configurations on the same structure, provides dual resolution capability. To test the system, we carried out CT scans of a plastic phantom with different source settings using both single-image and multi-image acquisition schemes at different spatial resolutions. In addition, CT scans of an ex-vivo mouse specimen were acquired at the best identified working conditions to demonstrate the

This article has been accepted for publication and undergone full peer review but has not been through the copyediting, typesetting, pagination and proofreading process, which may lead to differences between this version and the Version of Record. Please cite this article as doi: 10.1002/mp.14553

This article is protected by copyright. All rights reserved

Accepted Article

application of the presented system to small animal imaging.
Results: We found this system delivers good image quality, allowing for an efficient material separation and improving detail visibility in small animals thanks to the higher signal-to-noise ratio (SNR) of phase contrast with respect to conventional attenuation contrast. The system offers high versatility in terms of spatial resolution thanks to the double sample mask design integrated into a single scanner. The availability of both multi and single image acquisition schemes coupled with their dedicated retrieval algorithms, allows different working modes which can be selected based on user preference. Multi-image acquisition provides quantitative separation of the real and imaginary part of the refractive index, however it requires a long scanning time. On the other hand, the single image approach delivers the best material separation and image quality at all the investigated source settings with a shorter scanning time but at the cost of quantitativeness. Finally, we also observed that the single image approach combined with a high-power X-ray source may result in a fast acquisition protocol compatible with in-vivo imaging.

Accepted Article

This article is protected by copyright. All rights reserved

Accepted Article

Introduction

X-ray computed tomography (CT) is widely used in pre-clinical investigations thanks to its ability to provide high spatial resolution combined with short scanning times while using a relatively small scanner assembly[1,2]. However, the main limitation of X-ray CT in biological imaging is represented by the inherent low contrast when imaging soft tissues. This is an intrinsic limitation of the image formation mechanism, which is based on differences in attenuation coefficients. These are typically very small for soft tissues, yielding little to no contrast. However, a different image formation mechanism can be exploited in X-ray imaging. It relies on the decrement of the real part of the complex refractive index δ ($n = 1 - \delta + i\beta$), which is related to the phase shift suffered by an electromagnetic wave when it traverses a specimen[3,4,5]. Exploiting the phase shift may provide better contrast between soft tissues in the medically relevant range of X-ray energies (above 10 keV). This increased contrast is at the basis of the interest in this experimental technique. When combined with the coherence and high X-ray flux provided by synchrotron radiation sources, X-ray phase contrast imaging (XPCi) delivers images with very high soft tissue contrast, and spatial resolution that can match histology and transmission electron microscopy in several pre-clinical animal investigations, but with the advantage of non-destructive sample preparation[6,7,8,9]. Historically, the limited accessibility of synchrotron sources has limited the widespread use of XPCi. More recently, this has been overcome by several XPCi techniques based on conventional sources or by new source technologies[10,11,12,13,14]. Many laboratories that are currently developing phase detection techniques rely on optical elements (absorption or phase gratings). These approaches represent the most attractive solution towards commercially available XPCi scanners to serve the pre-clinical and medical communities[15]. In addition to phase contrast, these methods remain sensitive to the attenuation contrast and give access also to the small-angle scattering signal, which has, for example, potential applications in the detection of lung diseases[16,17]. In this manuscript, an implementation of the edge illumination phase detection method using a small table-top source is presented[11]. The requirement of a compact system imposes unavoidable constraints on the source's physical dimensions, and therefore on its output power. The system presented here has been tested on both a phantom and an ex-vivo mouse sample. In both cases, it provided good image performance and material separation due to the increased SNR of phase contrast over

This article is protected by copyright. All rights reserved

conventional attenuation contrast imaging. In addition, the system is versatile in terms of spatial resolution thanks to a double sample mask design, which is integrated into a single scanner. A single image acquisition combining phase and attenuation is also possible and represents the best compromise between image quality and scanning time. Finally, a comparison with another edge illumination system based on a more powerful source is used to qualitatively show the limits of the presented one.

Materials and Methods

Working principle

Edge illumination is an achromatic and incoherent X-ray phase detection method designed to work with conventional X-ray sources[11,18,19]. A schematic illustration of an edge illumination system is shown in Fig.1a. An X-ray beam is split into a series of beamlets by an absorption grating, referred to as the sample mask hereafter. These beamlets propagate to the detector where a second grating, the detector mask, is positioned so as to intercept a portion of each. When a sample is inserted into the beam path, refraction causes a shift of the beamlets away from or towards the corresponding pixel, resulting in a change in the recorded intensity. A quantitative relationship can be established between the recorded intensity change and refraction angle through the illumination curve (IC). The IC is obtained by scanning the masks relative to each other (usually the sample mask is moved while the detector mask is kept still) and measuring the intensity at each mask position. This is equivalent, from the detector point of view, to a shift of the beamlet. An example IC is shown in Fig.1c. The IC ranges from a minimum when the masks are mismatched, to a maximum when masks are aligned and each beamlet is fully transmitted. The illumination curve characterizes the phase sensitivity, and can be expressed analytically as:

$$IC(x) = (A_1 * S * A_2)(x) \tag{1}$$

where A_1 and A_2 are the sample and detector mask transmission functions, and S the source shape projected onto the detector plane. The $*$ symbol denotes the convolution operator. The projected focal spot size is given by $S_0(M-1)$ where M is the system magnification and S_0 the actual focal spot size. Remarkably, edge illumination is relatively tolerant against increasing projected source sizes, and it mainly requires that the beamlets are small enough

This article is protected by copyright. All rights reserved

Accepted Article

to partially illuminate a pixel[11,20]. Since the focal spot is usually Gaussian shaped, the IC can be approximated by a Gaussian function (see Gaussian fit in Fig.1c). In addition to refraction that shifts each beamlet according to the first derivative of the phase shift, edge illumination is also sensitive to X-ray attenuation that decreases the intensity of each beamlet depending on the imaginary part of the refractive index β. Thus, combining the effect of both processes on a beamlet, the intensity recorded by each pixel at position x in the detector column y can be expressed as:

$$I(x,y) = I_0 T(x,y) IC(x - \Delta x, y) \tag{2}$$

where I_0 is the beam intensity passing through the sample mask, $T(x,y)$ is the sample transmission function and $IC(x - \Delta x, y)$ is the illumination curve shifted because of refraction. The quantities $T(x,y)$ and Δx are related to the imaginary and real parts of the refractive index, respectively. In particular, $T(x,y) = e^{-\int \mu(x,y,z)dz}$, where $\mu = (4\pi/\lambda)\beta$ and λ is the wavelength of the incident radiation. Under the assumption of small angles, the shift Δx, can be related to the refraction angle by $\Delta\theta \sim \Delta x / z_{od}$, where z_{od} is the sample to detector distance. The refraction angle can then be related to the integrated real part of refractive index across the sample thickness by $\Delta\theta = \nabla_x \int \delta(x,y,z)dz$ where ∇_x is the gradient in the sample mask plane and perpendicular to the direction of the apertures. The disentanglement of these two effects is referred to as phase retrieval and requires the acquisition of at least two images[21]. In addition, if three images are acquired, the small angle scattering signal can be also retrieved[22]. A single image acquisition combining phase and attenuation channels into a hybrid image is also possible[23,24].

Edge illumination provides large flexibility in terms of spatial resolution. Spatial resolution is usually limited by sampling the specimen with discretely spaced beamlets and by signal diffusion into the scintillator layer if indirect detectors are used (cross-talk). The former is addressed by the acquisition and combination of several images taken while moving the sample in sub-pixel steps, covering all the missing portions in between apertures (dithered acquisition)[25]. The latter is addressed by using a skipped sample mask (see scheme in Fig.1b). In such a scheme, every other detector column (or more) is not illuminated, thus reducing signal diffusion[26]. The combination of skipped sample mask and dithered acquisition can bring the ultimate resolution down to the mask aperture size, regardless of the X-ray focal spot and physical detector pixel size[25]. However, such an increase in resolution comes at the

This article is protected by copyright. All rights reserved

Accepted Article

expense of an increase in the scanning time and dose delivered to the specimen.

System design

The compact system proposed here is based on a Hamamatsu L12161-07 Tungsten (W) microfocus source. The source size is about 15 μm when the small focus setting is used (see supplementary information, SI hereafter). In this working mode, the output power is limited to 10 W. Medium and large focus working modes are also available with a spot size ranging from 25 to 80 μm (see SI). However, the output power is variable, with a maximum achievable current of 500 μA for all voltages. The detector is a Hamamatsu C9732DK flat panel with an active area of 12×12 cm^2 and a square pixel size with 50 μm on a side[27]. The source to object (z_{so}) and object to detector (z_{od}) distances are both equal to 35 cm, providing a sample magnification equal to 2× that translates into a projected focal spot size equal to the actual focal spot. The masks have been manufactured by Microworks GmbH (Germany) by electroplating gold on a 400 μm thick graphite substrate. Gold absorbing septa are thicker than 120 μm from manufacture specifications. To exploit the flexibility offered by edge illumination in terms of spatial resolution, the presented system has been designed with a double sample mask, by arranging both a skipped and a non-skipped configurations on the same mask. This solution provides the advantages of a non-skipped mask in terms of scanning time, while also allowing for higher resolution scans by using the skipped mask, simply by a parallel translation of one optical element. A single non-skipped detector mask is always used. The detector mask pitch was 49μm, approximately matching the detector pixel size, while the aperture size was 24μm. The sample mask is scaled according to the system magnification, and therefore it has a pitch of 25 μm and 50 μm in the non-skipped and skipped configurations, respectively. The aperture size is 12 μm for both configurations.

Dose measurement

Absolute entrance dose measurements were acquired through a calibrated PTW Farmer 30010 ionization chamber positioned immediately downstream of the sample mask, where the sample is normally placed. Measurements are performed using a non-skipped mask. The results are extended to the skipped design assuming a perfectly absorbing gold layer. The validity of such an assumption decreases with increasing acceleration voltages due to the

This article is protected by copyright. All rights reserved

Accepted Article

increase of transmission through the sample mask. However, since higher energies contribute less to the delivered dose, it provides a reasonable estimate. The results are shown in Tab.1 as mean values with corresponding standard deviations.

Multi-contrast and multi-resolution acquisitions

The combination of skipped and non-skipped designs in a single mask, and the multi-contrast capability of edge illumination allow for different acquisition protocols. In multi-contrast acquisitions, the relationship provided by Eq.2 is used to separate attenuation and phase contrast channels. Assuming a Gaussian approximation for the illumination curve, Eq.2 can be written for any pixel and for any relative position s_i of the masks as:

$$I(x, y, s_i)/I_0 = T(x, y)\frac{A_{IC}}{\sqrt{2\pi\sigma_{IC}}}e^{-(s_i-\Delta x)^2/(2\sigma_{IC}^2)} \tag{3}$$

where A_{IC} and σ_{IC} are the amplitude and width of the IC without the sample. By acquiring two images on opposite sides of the illumination curve, i.e. at $x = \pm s_i$, a system of two equations is obtained, which can be solved at each pixel location for both $T(x, y)$ and Δx. The resulting solution quantitatively relates to the integrated μ and δ values across the sample thickness and can be fed to a computed tomography (CT) reconstruction algorithm, providing quantitative 3D maps of μ and δ within the sample[28]. This acquisition scheme can be used with both the non-skipped and skipped sample mask designs. In the first case the achieved spatial resolution will be limited by detector cross-talk, which is in the range of 100 μm, while in the second one it will be limited by the mask aperture size[15,25].

CT scans of a custom-made phantom consisting of three plastic materials, polymethyl methacrylate (PMMA), polystyrene (PS) and polypropylene (PP), have been performed using both configurations of the sample mask at different acceleration voltages, 40, 60, 80 kVp with constant power outputs of 10 W, using the small focus setting. A scan using the middle focus setting was also done for comparison, and is reported in the SI. It is worth noting that, in order to keep scanning times reasonably short for these acquisitions which require several images, the angular range was limited to 180 degrees. A parallel beam approximation has been assumed for CT reconstruction despite the cone beam geometry of our system. Such an assumption does not significantly impact spatial resolution considerations or quantitative estimations (see SI). The ASTRA toolbox has been used for efficient CT reconstruction[29].

This article is protected by copyright. All rights reserved

Accepted Article

For all CT scans, 200 projections have been taken and, to retrieve attenuation and phase contrast, two frames of 2 s exposure each have been acquired at all projection angles. These two frames were acquired on the opposing maximum slope positions of the illumination curve, located at about $\pm 4.2\ \mu m$ with respect to peak intensity (see Fig.1c). This corresponds to 400 images per scan, and therefore to an active scanning time of 800 seconds. When the skipped sample mask design was used, sub-pixel steps were also acquired at each IC position 1) by moving the sample five times by a distance of 10 μm, or 2) by moving it two times only by 25 μm, corresponding to a fifth or half of the period of the skipped sample mask design, respectively. While the latter is used for the purpose of comparison with the non-skipped design as the sampling points are the same in the two cases, the former provides a significant increase in resolution as it covers all the missing parts of the sample behind mask septa. In this case, the number of images per projection is increased to ten, and the total active scanning time to more than one hour. When only two dithering steps are taken, a total number of 800 images are acquired, doubling the scanning time compared to the acquisition with the non-skipped sample mask. Since the same exposure time per frame was used for both skipped and non-skipped mask acquisitions, using two dithering steps with the skipped mask system which features half the number of beamlets ultimately leads to the same dose being delivered to the sample. However, a change in the pixel statistic is expected as a consequence of the reduced cross-talk. Finally, it is worth mentioning that the actual scanning time can be longer, because some dead time is typically introduced after each movement of mask and sample. However, this can be minimised by means of accurate engineering of the data acquisition strategies. The need for several images due to both phase retrieval and dithering translates into an increase of the delivered dose. An entrance dose per image of (0.704 ± 0.004) mGy, (0.738 ± 0.004) mGy and (0.708 ± 0.002) mGy for the investigated acceleration voltages of 40, 60 and 80 kVp was measured when the non-skipped sample mask was used. Two images per projection have been acquired to retrieve phase and attenuation leading to a dose of less than 1.5 mGy per projection for all voltages, and of about 300 mGy for a whole CT scan, both using the non-skipped mask and the skipped mask with two dithering steps. When five dithering steps are acquired, the total dose per CT scan is increased to approximately 700 mGy.

A CT acquisition of an ex-vivo fresh mouse sample was also performed at the best working conditions, as identified from the analysis of the phantom scans. Specifically, the

This article is protected by copyright. All rights reserved

Accepted Article

non-skipped sample mask and an acceleration voltage of 40 kVp were used. A total number of 500 projections with 2 s exposure were acquired. In order to retrieve phase and attenuation two images at the maximum slope positions were acquired for each projection angle. The total entrance dose achieved was approximately 700 mGy.

In addition, to investigate the possible advantages provided by a more powerful source, a multi-contrast scan of the plastic phantom has been carried out using a different edge illumination setup, based on a similar non-skipped mask design and on the same detector, but using a different source and system geometry[15,30]. This system uses a Rigaku MicroMax 007 equipped with a rotating molybdenum (Mo) anode, operated at 40 kVp and 20 mA (800 W) and with a system magnification of 1.25×[15,30]. The results are shown in the SI.

The signal to noise ratio (SNR) has been calculated according to $SNR = \mu_{sample}/\sigma_{back}$, where μ_{sample} is the average value within the sample and σ_{back} is the standard deviation of the (air) background. A region of interest of 50×50 pixels was considered in all calculations.

Single image acquisition

A single image phase retrieval approach was used to speed up the acquisition[23,31]. This method assumes that the shift Δx is small enough to enable using a linear approximation of the IC. In addition, it also assumes that the sample is homogeneous and therefore that the μ and δ coefficients are proportional, i.e. $\gamma(E) = \delta(E)/\mu(E)$. It is worth noting that while the first assumption is valid in many cases, the latter is strictly true only for single material specimens. However, even if this condition is usually violated, the single image retrieval still provides good image quality with low noise, but at expense of quantitativeness[24]. Under these assumptions a hybrid image can be obtained as:

$$\int \mu(x,y,z)dz = -log\left[F^{-1}\left\{\frac{F\{I(x,y)/I_0\}}{1-2\pi \mathrm{i} z_{od} IC(s_i)/IC'(s_i)\gamma f_x}\right\}\right] \tag{4}$$

where $I(x,y)$ is the image acquired at sample mask position s_i, F denotes the Fourier transform, IC' is the first derivative of the IC and f_x are the spatial frequencies along x. For simplicity, the dependence of γ on energy was neglected. As this approach requires the acquisition of a single image, masks are not moved, and the sample can be continuously rotated (fly scan) while the detector acquires a sequence of frames, thus avoiding any dead time. However, since the sample is moved continuously, no intermediate dithering steps

This article is protected by copyright. All rights reserved

Accepted Article

can be acquired during the scan, and the resolution is limited by the detector point spread function. The previously described phantom was scanned using the single image acquisition. For this modality 400 projections over 360 degrees were acquired with an exposure time of 1 s each. Total entrance dose was below 150 mGy. The sample mask position was $-4.2\mu m$ from the peak intensity (see positions marked in Fig.1c), corresponding to the position of maximum slope. The retrieval algorithm has been applied to each individual projection after normalization and before CT reconstruction[23]. Finally, the fresh ex-vivo mouse sample has also been scanned using both the Hamamatsu W anode and the Rigaku Mo rotating anode systems mentioned above[15,30]. In both cases, 1000 projections over 360 degrees have been acquired with 1 second exposure. The total entrance dose was about 370 mGy for the CT scan acquired using the W source. In these cases, where scans over 360 degrees were available, CT reconstruction has been performed by means of the ASTRA toolbox assuming cone beam geometry[29].

Animal preparation

The scanned mouse was sacrificed at 10 days of age, in accordance with Schedule One of The Animals (Scientific Procedures) Act 1986 amendment regulations 2012, and imaged immediately after. No further preparation or fixation have been performed. The animal was placed into a plastic tube of approximately 1.5 cm in diameter, with empty spaces filled with agarose gel to prevent sample movements.

Accepted Article

This article is protected by copyright. All rights reserved

Accepted Article

Results

Multi-contrast and multi-resolution acquisitions

To test the performance of the proposed edge illumination system, all acquisition modalities discussed in the methods section have been first tested on the plastic phantom. The phantom has been scanned using both the non-skipped and skipped sample mask configurations at constant source power (10 W) in the multi-contrast acquisition mode providing both attenuation and phase contrast images by means of two-image phase retrieval[22,32]. The results for the attenuation contrast are shown in Fig.2. For both configurations (i.e. skipped and non-skipped sample mask) material 1 (PMMA) can be qualitatively distinguished from materials 2 and 3 (PS and PP) at the lower kVp setting. However, when the skipped sample mask is used, a lower SNR is found. This is visible from the graph reported in Fig.2b for PMMA. From a quantitative point of view, the three materials are barely distinguishable because of the high noise level. μ values equal to (0.49 ± 0.13) cm^{-1}, (0.32 ± 0.13) cm^{-1} and (0.30 ± 0.13) cm^{-1} are found for PMMA, PS and PP, respectively, when a non-skipped mask and 40 kVp are used. A good agreement with the expected values of 0.46, 0.34 and 0.29 cm^{-1} is found. Similar values are also found for the skipped mask (see SI). However, the standard deviation is approximately 30% of the average values. This is illustrated by the histograms reported for the 40 kVp setting for both mask configurations in the inset of Fig.2a. In both cases, the histogram features a single large peak, with an asymmetric tail on the right-hand side due to the higher μ value expected for PMMA. When the voltage is increased to the upper value of 80 kVp, a decrease in the signal to noise ratio can be observed as shown by the SNR graph (see Fig.2b). This is again in agreement with the decrease of the μ coefficient with increasing X-ray energy. In addition, as the voltage increases, a larger deviation from the expected value is observed for the experimentally extracted value of μ for all materials (see SI). Finally, the SNR of the non-skipped configuration remains higher than the skipped one across all the investigated voltages, as shown in the graph in Fig.2b

A set of phase contrast CT slices are shown in Fig.3a; the corresponding grey level distribution histograms for all materials at 40 kVp is shown in the insets. The SNR for PMMA as a function of the tube voltage is shown in Fig.3b. The non-skipped sample mask shows a higher SNR level compared to the skipped one (see graph in Fig.3b). This difference

This article is protected by copyright. All rights reserved

is again maintained across all the investigated voltages, while the SNR is found to decrease for both configurations according to the decrease in the δ coefficient with increasing X-ray energy. As visible in the histograms in Fig.3a, the non-skipped sample mask allows three peaks to be distinguished in the grey level distribution, while in the skipped configuration these mix in a single, broad peak, therefore providing a worse separation between the materials. From a quantitative point of view, a δ value equal to $(3.88 \pm 0.26) \cdot 10^{-7}$, $(2,93 \pm 0.19) \cdot 10^{-7}$ and $(2.55 \pm 0.20) \cdot 10^{-7}$ are found for PMMA, PS and PP, respectively, using the non-skipped mask at 40 kVp. The experimental values appear underestimated compared to the expected theoretical values of $4.17 \cdot 10^{-7}$, $3.72 \cdot 10^{-7}$ and $3.55 \cdot 10^{-7}$. Again, the mismatch increases with the acceleration voltage (see SI).

The previous considerations show that the lowest investigated acceleration voltage and the non-skipped sample mask provide the best results in terms of SNR when multi-contrast imaging is used. To demonstrate the performance of the selected configuration on a real sample, the chest region of a fresh mouse was scanned ex-vivo. Results are shown in Fig.4. Multi-contrast planar radiographic images and CT slices are shown in Fig.4a, d and Fig.4b-c, e-f, respectively. In the attenuation radiography reported in Fig.4a the skeleton is evident as well as the lungs (see red arrow), which appear white because of their lower density compared to the surrounding tissues. Air bubbles are also seen in the bowel region at the bottom of the image. Conversely, in the differential phase contrast radiography reported in Fig.4d, the bone-tissue interface is hardly visible, and the full respiratory tract, up to the trachea, can be easily detected because it is not obscured by the spinal cord like in the attenuation radiography (see red arrow in Fig.4d). In addition, CT slices are reported in Fig.4b,c and in Fig.4e,f for attenuation and phase contrast channels, respectively. The attenuation channel allows a good visualisation of the lungs inside the rib cage as well as details inside the lung tissue, including some of the airways branches. However, the phase contrast channel provides a better view of a range of fine details of the lung structure, including airways and separation boundaries between different lobes of the lungs (see blue arrows in Fig.4f).

The additional availability of a skipped sample mask provides flexibility in terms of resolution, allowing multi-resolution capability within a multi-contrast acquisition. In order to provide a qualitative comparison in terms of spatial resolution when skipped or non-skipped sample masks are used for multi-contrast imaging, the plastic phantom has been imaged in both modalities. A defect found inside one of the phantom spheres is used in the compari-

This article is protected by copyright. All rights reserved

Accepted Article

son as discussed in relation to Fig.5a and b for the attenuation and phase contrast channels, respectively. The comparison between the appearance of the defect in the two contrast channels highlights the advantage provided by phase contrast. In the attenuation channel, the increase in resolution provided by the skipped mask and dithering acquisition is rendered negligible by the higher noise compared to the lower resolution image (see Fig.5a). This finding agrees with consistently lower SNR values observed for the skipped mask configuration (see Fig.2 and Fig.3), and must be compensated by an increase in the exposure time in order to get the same pixel statistics of the non-skipped acquisition. On the other hand, the inherent higher SNR provided by phase contrast compensates for the higher noise when the skipped sample mask is used. Therefore, the increase in resolution introduced by the skipped mask configuration, can be clearly appreciated, as shown in Fig.5b. In particular, several details (highlighted by red arrows in Fig.5b) are resolved, while they appear blurred in the low-resolution phase contrast image acquired with the non-skipped mask.

Single image acquisition

To test the performance of the presented system when single image acquisition is used, a CT scan of the same phantom has been acquired using 40,60 and 80 kVp at constant 10W power. The images and associated grey level histograms, are reported in Fig.6. At 40 kVp all the materials can be easily distinguished. The grey level distributions show three well separated peaks, where the rightmost one corresponds to PMMA, the central one to PS and the leftmost to PP. When the voltage is increased, the SNR decreases and the PMMA grey levels (rightmost peak) approaches the values for PP and PS; however, it remains well separated even at 80 kVp.

To exploit the high image quality provided by the single image acquisition method, a CT scan of the same mouse has been acquired using this modality with results reported in Fig.7. The Fig.7a and b show coronal and transverse sections of the mouse chest region, respectively. Lungs within the rib cage are clearly visualized including branches of the airways. In addition, the spongy appearance of the lung tissue is highlighted by the magnified inset in Fig.7b. Finally, in Fig.7c a 3D rendering of the imaged chest region is shown to provide a better visualization of the volumetric arrangement of the airways. The results shown in Fig.7 have been obtained using a low power source (10 W) in order to keep the system

This article is protected by copyright. All rights reserved

Accepted Article

compact. However, if reducing the scanning time becomes critical, it may be possible to replace the above-mentioned source with a rotating anode source with higher power output. The result of a test using an edge illumination system based on a Mo rotating anode X-ray source operated at 40 kVp and 20 mA (800 W) is shown in Fig.8. It is worth noting that this test was carried out for a qualitative comparison only, since a different source anode (Mo) and system geometry were used[15,30]. However, some conclusions can be still drawn from it, since the mean energies for W and Mo anodes at 40 kVp voltage are not exceedingly different (25 and 22 keV for W and Mo, respectively) . Remarkably, a comparable level of detail is visualized in both cases, but a better separation between different tissues is obtained with the more powerful Mo source. This can be easily appreciated by focusing on the subcutaneous fat layers that are barely distinguished with the 10 W source (see Fig.8a), but become evident when the 800 W source is used (see Fig.8b). This is also confirmed by the line profiles extracted across fat and muscle tissues for both images, reported in the graph in Fig.8c.

Discussion

The requirement of a compact system imposed some constraints on the physical source size preventing the use of the high-power rotating anode sources normally used to compensate for the flux reduction caused by the absorption masks. Our results show the level of performance achievable when edge illumination is implemented with a low power X-ray source (10 W) while keeping a reasonably short scanning time (within one hour). We found a poor material separation in the attenuation contrast channel with both the skipped and non-skipped sample mask configurations. A comparison between CT slices acquired both with the higher power output available in the medium focus mode (20 W), and with a more powerful source (800 W), reveals that the key reason behind the inability to distinguish the investigated materials is the poor SNR provided by the combination of low attenuation cross section and low source power output (see SI). A better distinction between the materials is obtained with phase contrast thanks to the higher phase shift coefficient delivering a higher SNR, which compensates for the low source power output (see SI). From a quantitative point of view, a good agreement between the experimental and theoretical values of μ is found for the lower investigated voltages using both mask configurations (see SI). On the other hand, a

This article is protected by copyright. All rights reserved

Accepted Article

systematic underestimation of the δ value is found (see SI), which may be explained by a non-perfect sampling of the phase peak, negatively affecting the quantitative value of the integrated differential phase image[26,33,34]. A deviation from the expected value is also found for both coefficients at the highest investigated voltage, which may be due to an oversimplified model of the system response[35]. The best performance for the attenuation contrast is achieved with the maximum available current regardless of the source size, as can be expected because the SNR is only related to photon flux. On the other hand, image quality in phase contrast can be improved both by increasing the system phase sensitivity and by increasing the photon flux. While the latter is easily achievable by increasing the source current, attention must be paid to avoid an excessive increase in the spot size, which may cancel out the advantages provided by the higher photon statistics (see SI). Therefore we found that, with the used source, the best image quality in both channels is obtained with the lower investigated voltage of 40 kVp, which allows for the highest current while keeping a small focus size. This configuration provided good image quality of a mouse sample despite the low source output, enhancing the visibility of lung structures and of the airways thanks to phase contrast.

The presented system combines the inherent multi-contrast capability of edge illumination with a flexible resolution thanks to a new design of the sample mask. Importantly, switching from low to high resolution (and vice versa) involves only a parallel translation of an optical element with no change in the system components and minimal system realignment. The combination of skipped sample mask and dithering acquisition allows reaching a resolution equal to the mask aperture size[25,26]. However, we observed that the skipped mask provides a lower SNR compared to the non-skipped one, due to the reduction (of a factor two) in the available flux caused by the former. While the beamlets eliminated by the skipped mask have a negative impact on spatial resolution, they contribute to the overall SNR[26]. Therefore, a longer integration time per projection is required to match the pixel statistics obtained with the non-skipped sample mask. We observed that, if the time per projection is kept the same for the skipped and non-skipped sample masks, the improvement in spatial resolution is clearly observable only in the phase contrast channel, as in the attenuation one the increased noise can render the benefits negligible. In addition, when dithered acquisitions are performed, the total scanning time is increased by a factor at least equal to the number of acquired dithering steps. For the system presented here, this translates into a

This article is protected by copyright. All rights reserved

Accepted Article

five-fold increase in the overall scanning time for high-resolution multi-contrast acquisitions. In general, the increase in the scanning time required by all the multi-image acquisition modes represents the main limitation to their applications to animal imaging, as it makes in-vivo use more difficult. For the same reason, clinical translation becomes more difficult because of the increased delivered dose levels.

So long as an appropriate retrieval algorithm is used, edge illumination works also in single image acquisition mode like free space propagation[23,31]. When using single image acquisition, the limitations in terms of contrast and SNR observed with the multi-contrast acquisition are overcome. The advantages of both phase and attenuation are combined into an image with good material separation and high SNR, indicating this method as potentially the best choice when low power sources are used. However, the obtained results are not quantitative, since different δ/μ ratios should be used to locally retrieve each interface correctly[36]. This method is therefore preferable when the main objective is high image quality and quantitative measurements are not required. Single image CT scans of the ex-vivo mouse sample showed fine structures in the lungs and offers a more straightforward implementation for in-vivo applications thanks to the use of a more powerful source, as shown by the comparison with an edge illumination system based on a 800 W X-ray source. However, the comparison between results obtained with the two sources presented in this paper should only be considered qualitative, since anode materials and system geometry were different. In the specific case of an 800 W source, it would be possible to reduce the exposure time by up to a factor of 80 whilst keeping a good image quality. Such a reduction in integration time per image would significantly facilitate the translation of edge illumination into in-vivo preclinical imaging in the near future.

Conclusions

An implementation of the edge illumination phase detection scheme using a low power, microfocus source and a combined skipped/non-skipped sample mask design has been presented and tested using a plastic phantom and a fresh ex-vivo mouse. Such a design allows significant versatility in a compact system, as it allows for several acquisition schemes. The multi-contrast approach provides two different contrast channels capable of delivering complementary quantitative information at different spatial resolutions. Phase imaging, with its

This article is protected by copyright. All rights reserved

Accepted Article

inherently higher SNR, provides a superior image quality compared to attenuation. Where speed is the main concern, single image acquisition provides a high SNR and good image quality by trading off on quantitativeness. The use of a more powerful source has also been tested for a qualitative comparison. The results highlight the ability of phase-contrast imaging to boost image quality, and how this can be particularly important when only a low source output is available. When the constraints on the physical source dimensions can be removed, the combination of phase sensitivity and high flux make fast in-vivo applications more easily achievable.

Acknowledgments

This research was supported by PerkinElmer Inc. and EPSRC grant EP/L001381/1. M.Endrizzi was supported by the Royal Academy of Engineering under the RAEng Research Fellowships scheme. A.Olivo was supported by the Royal Academy of Engineering under the Chairs in Emerging Technologies schemes. We thank Dr. Gibril K.Kallon, from the Advanced X-ray Imaging group of the Department of Medical Physics and Biomedical Engineering, University College London, for the invaluable discussions and support while writing the manuscript. We also thank Dr. Ian Buchanan from the Advanced X-ray Imaging group of the Department of Medical Physics and Biomedical Engineering, University College London for the support during the dose measurements.

Conflicts of interest

The authors have no relevant conflicts to disclose.

References

[1] R. Mizutani and Y. Suzuki, X-ray microtomography in biology, Micron **43**, 104–115 (2012).

[2] D. Clark and C. Badea, Micro-CT of rodents: state-of-the-art and future perspectives, Physica medica **30**, 619–634 (2014).

This article is protected by copyright. All rights reserved

Accepted Article

Accepted Article

[3] A. Bravin, P. Coan, and P. Suortti, X-ray phase-contrast imaging: from pre-clinical applications towards clinics, Physics in Medicine & Biology **58**, R1 (2012).

[4] A. Snigirev, I. Snigireva, V. Kohn, S. Kuznetsov, and I. Schelokov, On the possibilities of x-ray phase contrast microimaging by coherent high-energy synchrotron radiation, Review of scientific instruments **66**, 5486–5492 (1995).

[5] A. Momose and J. Fukuda, Phase-contrast radiographs of nonstained rat cerebellar specimen, Medical physics **22**, 375–379 (1995).

[6] A. Cedola et al., X-ray phase contrast tomography reveals early vascular alterations and neuronal loss in a multiple sclerosis model, Scientific reports **7**, 1–11 (2017).

[7] L. Massimi et al., Exploring Alzheimer's disease mouse brain through X-ray phase contrast tomography: From the cell to the organ, NeuroImage **184**, 490–495 (2019).

[8] L. Massimi et al., Characterization of mouse spinal cord vascular network by means of synchrotron radiation X-ray phase contrast tomography, Physica Medica **32**, 1779–1784 (2016).

[9] M. Fratini et al., Simultaneous submicrometric 3D imaging of the micro-vascular network and the neuronal system in a mouse spinal cord, Scientific reports **5**, 8514 (2015).

[10] H. H. Wen, E. E. Bennett, R. Kopace, A. F. Stein, and V. Pai, Single-shot x-ray differential phase-contrast and diffraction imaging using two-dimensional transmission gratings, Optics letters **35**, 1932–1934 (2010).

[11] A. Olivo and R. Speller, A coded-aperture technique allowing x-ray phase contrast imaging with conventional sources, Applied Physics Letters **91**, 074106 (2007).

[12] F. Pfeiffer, T. Weitkamp, O. Bunk, and C. David, Phase retrieval and differential phase-contrast imaging with low-brilliance X-ray sources, Nature physics **2**, 258–261 (2006).

[13] M. Krenkel, M. Töpperwien, C. Dullin, F. Alves, and T. Salditt, Propagation-based phase-contrast tomography for high-resolution lung imaging with laboratory sources, AIP Advances **6**, 035007 (2016).

This article is protected by copyright. All rights reserved

Accepted Article

[14] L. Brombal et al., Monochromatic propagation-based phase-contrast microscale computed-tomography system with a rotating-anode source, Physical Review Applied **11**, 034004 (2019).

[15] L. Massimi et al., Laboratory-based x-ray phase contrast CT technology for clinical intra-operative specimen imaging, in *Medical Imaging 2019: Physics of Medical Imaging*, volume 10948, page 109481R, International Society for Optics and Photonics, 2019.

[16] A. Yaroshenko et al., Pulmonary emphysema diagnosis with a preclinical small-animal x-ray dark-field scatter-contrast scanner, Radiology **269**, 427–433 (2013).

[17] P. Modregger, T. P. Cremona, C. Benarafa, J. C. Schittny, A. Olivo, and M. Endrizzi, Small angle x-ray scattering with edge-illumination, Scientific reports **6**, 30940 (2016).

[18] M. Endrizzi, F. Vittoria, L. Rigon, D. Dreossi, F. Iacoviello, P. Shearing, and A. Olivo, X-ray phase-contrast radiography and tomography with a multiaperture analyzer, Physical review letters **118**, 243902 (2017).

[19] M. Endrizzi, F. A. Vittoria, G. Kallon, D. Basta, P. C. Diemoz, A. Vincenzi, P. Delogu, R. Bellazzini, and A. Olivo, Achromatic approach to phase-based multi-modal imaging with conventional x-ray sources, Optics express **23**, 16473–16480 (2015).

[20] A. Olivo, K. Ignatyev, P. Munro, and R. Speller, Design and realization of a coded-aperture based X-ray phase contrast imaging for homeland security applications, Nuclear Instruments and Methods in Physics Research Section A: Accelerators, Spectrometers, Detectors and Associated Equipment **610**, 604–614 (2009).

[21] M. Endrizzi and A. Olivo, Absorption, refraction and scattering retrieval with an edge-illumination-based imaging setup, Journal of Physics D: Applied Physics **47**, 505102 (2014).

[22] M. Endrizzi, P. C. Diemoz, T. P. Millard, J. Louise Jones, R. D. Speller, I. K. Robinson, and A. Olivo, Hard X-ray dark-field imaging with incoherent sample illumination, Applied Physics Letters **104**, 024106 (2014).

[23] P. Diemoz, C. Hagen, M. Endrizzi, M. Minuti, R. Bellazzini, L. Urbani, P. De Coppi, and A. Olivo, Single-shot x-ray phase-contrast computed tomography with nonmicrofocal laboratory sources, Physical Review Applied **7**, 044029 (2017).

This article is protected by copyright. All rights reserved

Accepted Article

[24] C. K. Hagen, O. Roche i Morgó, and A. Olivo, Predicting the noise in hybrid (phase and attenuation) x-ray images acquired with the edge illumination technique, Medical Physics (2020).

[25] P. C. Diemoz, F. A. Vittoria, and A. Olivo, Spatial resolution of edge illumination x-ray phase-contrast imaging, Optics express **22**, 15514–15529 (2014).

[26] K. Ignatyev, P. Munro, R. Speller, and A. Olivo, Effects of signal diffusion on x-ray phase contrast images, Review of Scientific Instruments **82**, 073702 (2011).

[27] M. Endrizzi, P. Oliva, B. Golosio, and P. Delogu, CMOS APS detector characterization for quantitative X-ray imaging, Nuclear Instruments and Methods in Physics Research Section A: Accelerators, Spectrometers, Detectors and Associated Equipment **703**, 26–32 (2013).

[28] C. Hagen, P. Munro, M. Endrizzi, P. Diemoz, and A. Olivo, Low-dose phase contrast tomography with conventional x-ray sources, Medical physics **41**, 070701 (2014).

[29] W. Van Aarle, W. J. Palenstijn, J. De Beenhouwer, T. Altantzis, S. Bals, K. J. Batenburg, and J. Sijbers, The ASTRA Toolbox: A platform for advanced algorithm development in electron tomography, Ultramicroscopy **157**, 35–47 (2015).

[30] G. Havariyoun et al., A compact system for intraoperative specimen imaging based on edge illumination X-ray phase contrast, Physics in Medicine & Biology **64**, 235005 (2019).

[31] D. Paganin, S. C. Mayo, T. E. Gureyev, P. R. Miller, and S. W. Wilkins, Simultaneous phase and amplitude extraction from a single defocused image of a homogeneous object, Journal of microscopy **206**, 33–40 (2002).

[32] M. Endrizzi and A. Olivo, Absorption, refraction and scattering retrieval with an edge-illumination-based imaging setup, Journal of Physics D: Applied Physics **47**, 505102 (2014).

[33] C. Hagen, P. Diemoz, M. Endrizzi, and A. Olivo, The effect of the spatial sampling rate on quantitative phase information extracted from planar and tomographic edge

This article is protected by copyright. All rights reserved

illumination x-ray phase contrast images, Journal of Physics D: Applied Physics **47**, 455401 (2014).

[34] C. Hagen, P. Coan, A. Bravin, A. Olivo, and P. Diemoz, A continuous sampling scheme for edge illumination x-ray phase contrast imaging, Journal of Applied Physics **118**, 054901 (2015).

[35] P. R. Munro and A. Olivo, X-ray phase-contrast imaging with polychromatic sources and the concept of effective energy, Physical Review A **87**, 053838 (2013).

[36] A. Zamir, P. C. Diemoz, F. A. Vittoria, C. K. Hagen, M. Endrizzi, and A. Olivo, Edge illumination X-ray phase tomography of multi-material samples using a single-image phase retrieval algorithm, Optics express **25**, 11984–11996 (2017).

Accepted Article

This article is protected by copyright. All rights reserved

Accepted Article

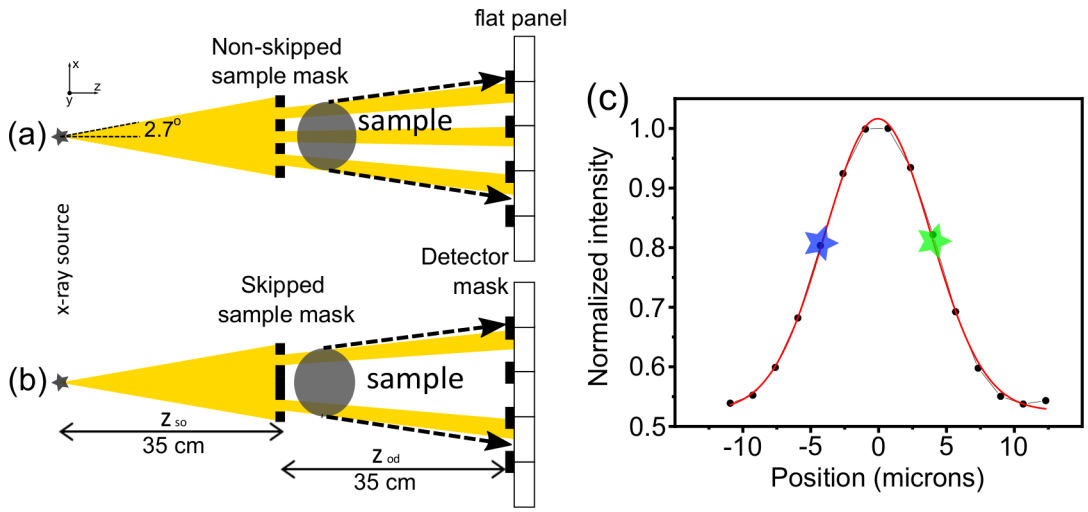

Figure 1: Panel (a) shows a top view sketch of the edge illumination setup when a non-skipped sample mask is used. A beamlet is created for each detector column. Panel (b) shows a top view sketch of the edge illumination setup when a skipped sample mask is used. In this configuration, one detector column is not illuminated. Panel (c) shows an example illumination curve obtained with the non-skipped edge illumination system presented in this manuscript. Maximum slope positions, where phase sensitivity is maximised, are located at $\pm 4.2 \mu m$ from the peak intensity and marked by coloured stars. The gaussian fit is indicated by the red curve.

This article is protected by copyright. All rights reserved

Table 1: Absolute dose measurements at the different investigated acceleration voltages.

Voltage (kVp)	Current (μA)	Dose (mGy/s)
40	250	0.352 ± 0.002
60	166	0.369 ± 0.002
80	125	0.354 ± 0.001

Accepted Article

This article is protected by copyright. All rights reserved

Accepted Article

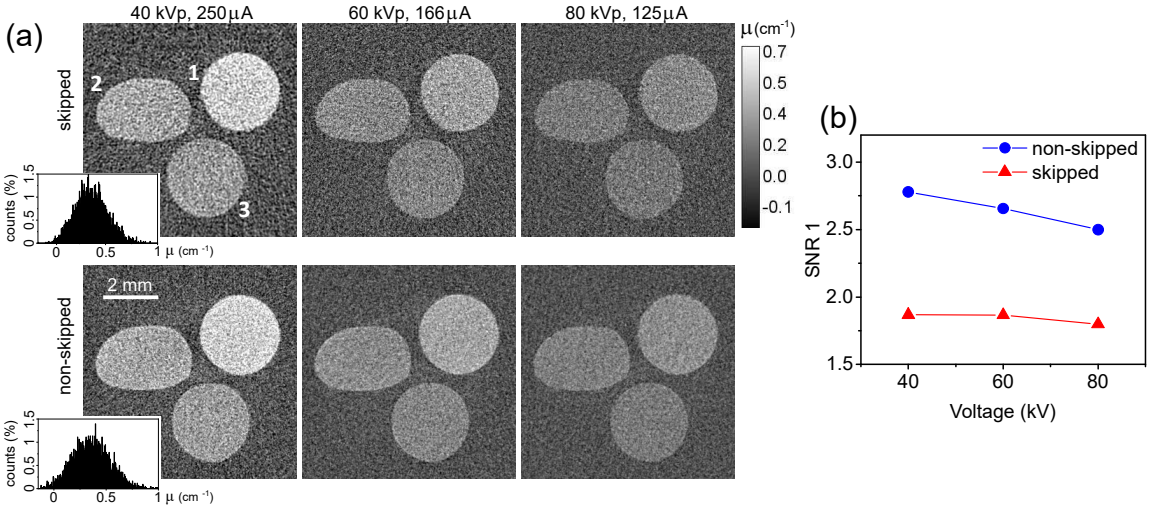

Figure 2: Panel (a) shows a comparison of retrieved attenuation contrast CT slices of the phantom for both mask configurations, i.e. skipped and non-skipped, at different acceleration voltages ranging from 40 kVp to 80 kVp and at a constant source power of 10 W. Histograms for all the spheres are shown for both mask configurations at the lowest voltage. Panel (b) reports the SNR values calculated for both sample mask configurations for material 1. Material labelled as 1 is PMMA, 2 is PS and 3 is PP.

This article is protected by copyright. All rights reserved

Accepted Article

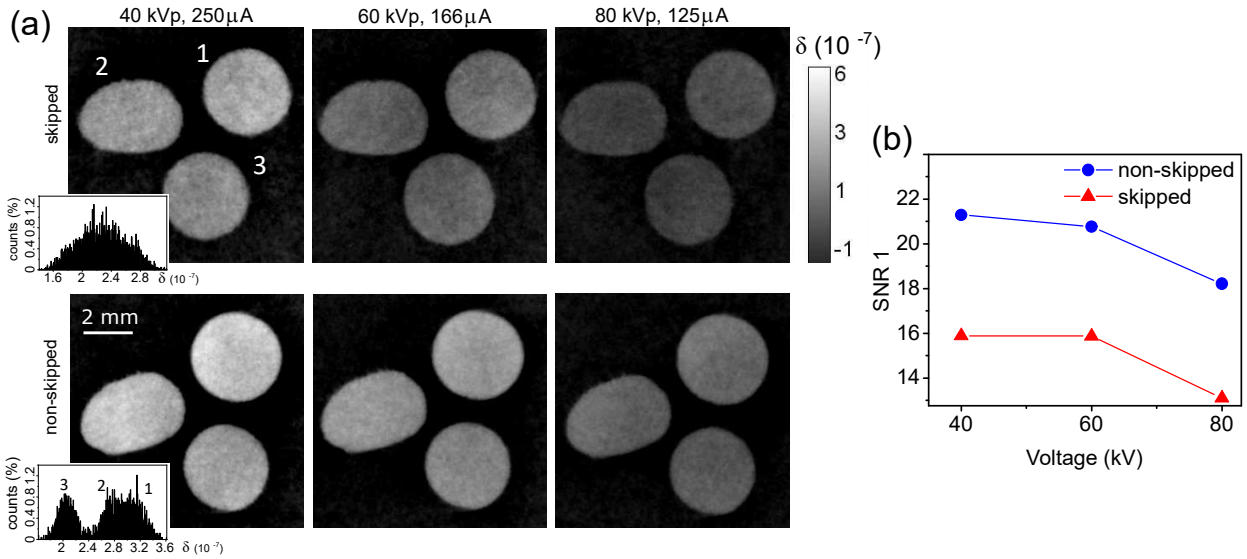

Figure 3: Panel (a) shows a comparison of retrieved phase contrast CT slices of phantom for both mask configurations at different acceleration voltages ranging from 40 kVp to 80 kVp. For each voltage maximum achievable current was used. Grey level distributions for each sphere and both mask configurations at the lowest voltage are shown in the inset. Panel (b) reports the SNR for each configuration for material 1. Material labelled by 1 is PMMA, 2 is PS and 3 is PP.

This article is protected by copyright. All rights reserved

Accepted Article

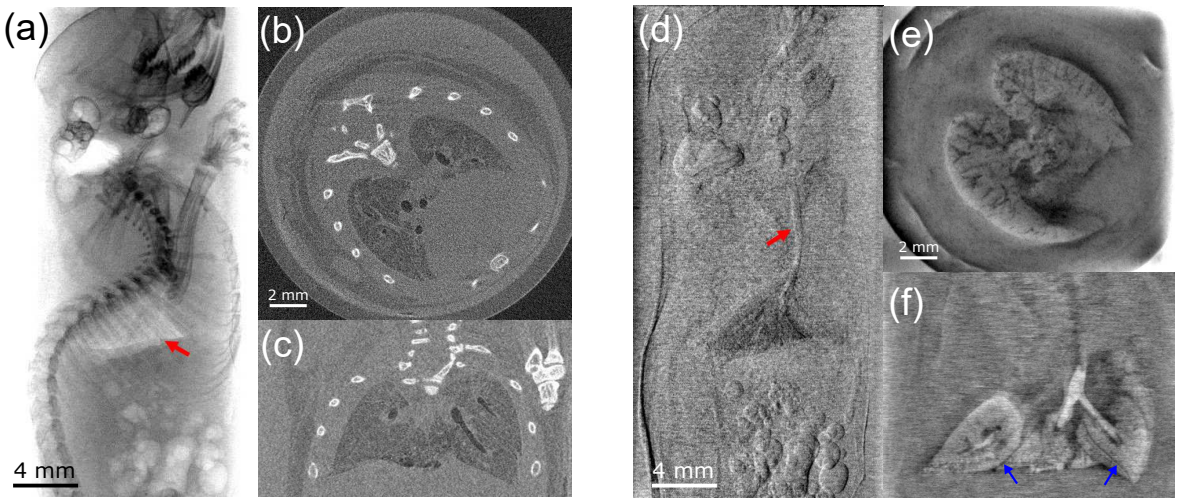

Figure 4: Multi-contrast planar radiographic images and CT slices of a mouse chest region. Panel (a) and (d) show the retrieved attenuation and differential phase radiography, respectively. Panels (b),(c) and (e),(f) show transverse and coronal attenuation and integrated phase contrast CT slices, respectively. The red arrow in panel (a) points at the lungs inside the rib cage. In panel (d) the red arrow points at the trachea, while the blue arrows in panel (f) highlight separations between different lobes of the lungs.

This article is protected by copyright. All rights reserved

Accepted Article

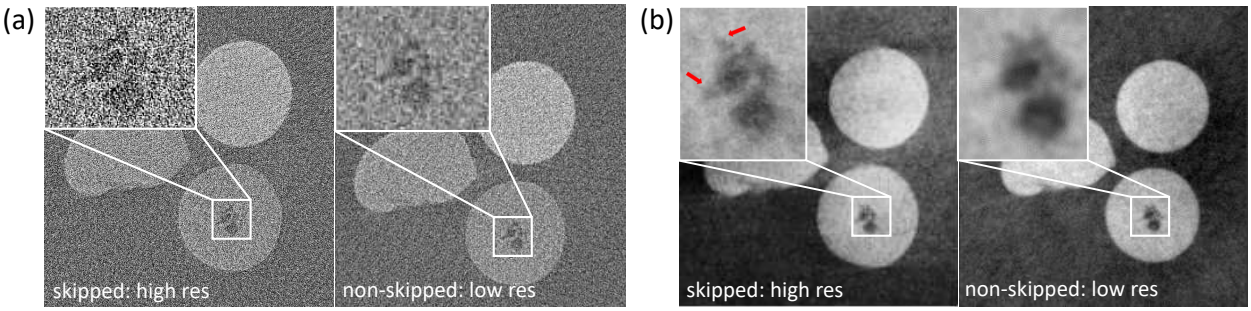

Figure 5: Comparison between high- and low-resolution multi-contrast acquisitions. In the first case a skipped sample mask is used in combination with five dithering steps, while in the latter a non-skipped sample mask is used. Panel (a) and (b) show the comparison for the attenuation and phase contrast channels, respectively. In the insets, a magnified detail of a defect in the PP sphere is shown and used for comparison purposes.

This article is protected by copyright. All rights reserved

Accepted Article

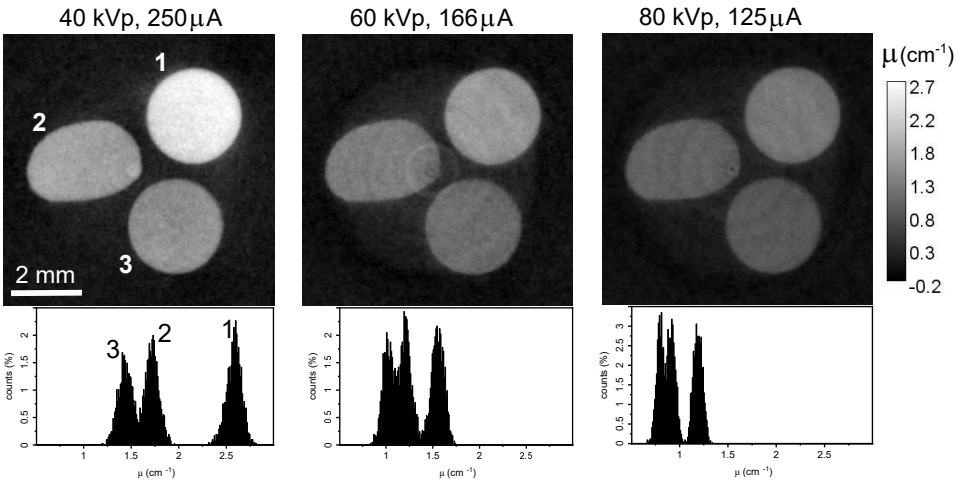

Figure 6: Comparison of single image acquisition CT slices of the plastic phantom for the non-skipped mask configuration at 40 kVp, 60 kVp and 80 kVp. For each image, the grey levels histogram distributions of the different materials are shown. Material 1 is PMMA, 2 is PS and 3 is PP.

This article is protected by copyright. All rights reserved

Accepted Article

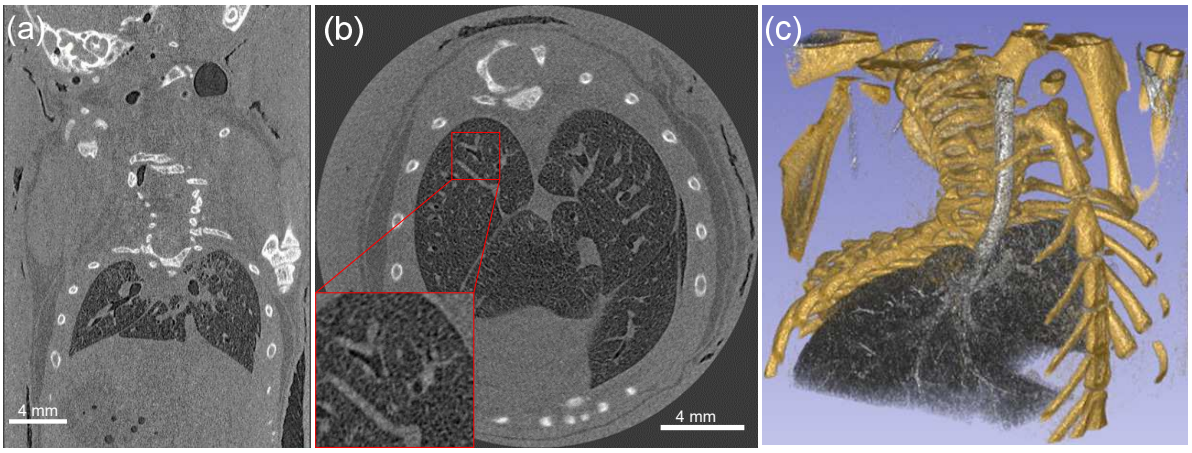

Figure 7: Single image CT acquisition of the mouse chest region. Panels (a) and (c) show a coronal and a transverse slice, respectively. A magnified region inside lung tissue showing part of the airways and the structure of the lung tissue is also shown as an inset. Panel (c) shows a 3D rendering of the chest region including rib cage, trachea and lungs.

This article is protected by copyright. All rights reserved

Accepted Article

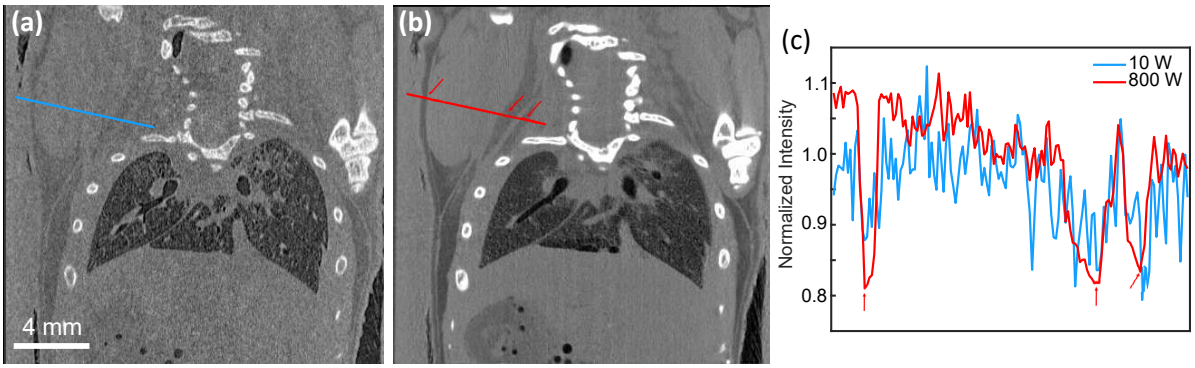

Figure 8: Comparison of a CT coronal slice of mouse chest region obtained with single image acquisition with a 10 W source in panel (a) and an 800 W source in panel (b). Panel (c) shows line profile across fat and muscle tissues for both acquisitions. Red arrows point at different layers of fat tissue observed in panel (b) and hardly visible in panel (a).

This article is protected by copyright. All rights reserved

Table 1

Voltage (kVp)	Current (μA)	Dose (mGy/s)
40	250	0.352 ± 0.002
60	166	0.369 ±0.002
80	125	0.354 ± 0.001

Absolute dose measurements at the different investigated acceleration voltages.

Accepted Article

This article is protected by copyright. All rights reserved